# Random Graphene Metasurfaces: Diffraction Theory and Giant Broadband Absorptivity

Andrey Novitsky,[1,2,*] Alesia Paddubskaya,[1] Isaac Appiah Otoo,[3] Markku Pekkarinen,[3] Yuri Svirko,[3] and Polina Kuzhir[3]

[1] *Institute for Nuclear Problems of Belarusian State University, Bobruiskaya Str. 11, 220006 Minsk, Belarus*

[2] *Department of Theoretical Physics and Astrophysics, Belarusian State University, Nezavisimosti av. 4, 220030 Minsk, Belarus*

[3] *Department of Physics and Mathematics, Institute of Photonics, University of Eastern Finland, P.O. Box 111, FI-80101 Joensuu, Finland*

(Received 16 February 2022; revised 28 March 2022; accepted 5 April 2022; published 21 April 2022)

We introduce a diffraction-theory-inspired analytical description of the metasurface comprising an array of graphene subwavelength hemispheres. Our theory describes light interaction with the random metasurface, in which the periodicity is broken by accidentally damaged meta-atoms in the nodes of a two-dimensional periodic lattice. Both numerical modeling and experiments show that such a nanometer-thin metasurface possesses giant broadband absorption in the terahertz spectral range that remains intact, even when a substantial portion of meta-atoms, i.e., graphene hemispheres, is damaged. Moreover, defective fabrication of graphene free-standing metasurface may enhance the absorptive properties.

DOI: 10.1103/PhysRevApplied.17.044041

## I. INTRODUCTION

Tailoring of the surface impedance gave rise to metasurfaces, which are two-dimensional subwavelength structures capable of controlling the amplitude, phase, and polarization of electromagnetic waves [1–5]. Subwavelength thin metasurfaces outperform volumetric metamaterials, heralding their potential use for beam steering and focusing via phase management of the reflected and transmitted waves. This enables numerous applications of metasurfaces, including as bandpass and bandstop filters, narrowband perfect absorbers, polarizers, lenses, and holography [2]. The discovery of phase-gradient metasurfaces (also referred to as frequency-selective surfaces) capable of controlling the phase in the full range from 0 to $2\pi$ has led to the generalization of reflection and refraction laws [6], while metasurfaces comprising spatially varying orientations of subwavelength scatterers enable exploitation of the effect of the Pancharatnam-Berry phase [7]. Metasurfaces with long-range order in the meta-atom array can be described in terms of multipole moments (usually dipole moments) of unit cells or equivalent surface impedances. In particular, in the so-called Huygens' metasurface [8], the dielectric and magnetic dipole moments of the unit cell are arranged in such a way that the reflected wave is suppressed.

Graphene-based metasurfaces have attracted attention because control of the graphene-surface conductivity (change of the Fermi energy) by chemical or electrical doping may enable tunability over a wide spectral range [9]. Full control of the graphene metasurface can be achieved if the voltage is independently applied to individual unit cells [10]. A graphene metasurface designed to give a $0-2\pi$ phase shift due to the interplay between plasmon and Fabry-Perot resonances can be employed for cloaking, illusion, and focusing [11]. Curiously, graphene ribbons may act as a platform for Moiré hyperbolic metasurfaces, demonstrating a topological transition at magic angles, field canalization, and the plasmonic spin-Hall effect [12].

In spite of its negligible thickness, graphene can be used to design effective absorbers in the terahertz (THz) domain. In Ref. [13], omega-shaped graphene patterns were designed for use as a wide-incident-angle absorber over more than 1-THz bandwidth. A wide absorption bandwidth is achievable in a multilayer system with an embedded graphene sheet [14], with perfect absorption for a specific incident angle and layer thickness. The broadband absorption in the THz range can be realized in planar structures composed of metal and dielectric layers [15] or layers of graphene with modulated chemical potential [16], as well as in singular graphene gratings [17].

Subwavelength periodicity of metasurfaces is advantageous from the fabrication and theoretical modeling perspectives, but not necessary. Here, we propose a closed-form description of metasurfaces comprising different unit cells randomly distributed on the plane. Such a two-dimensional structure can be called a "random" metasurface. This term was proposed in Ref. [18] to describe the

*andreyvnovitsky@gmail.com

 

properties of randomly oriented nanoscale gold bars in the near-infrared frequency range.

Here, we investigate random graphene metasurfaces comprising different types of unit cells: hemispheres, volcanos, and holes. Assuming that there is no electromagnetic coupling between unit cells, we reduce the problem of light interaction with such random metasurfaces to light scattering by unit cells. We employ the developed approach to a free-standing graphene metasurface and reveal that suppression of meta-atom's dipole moment results in nearly perfect absorption over a wide THz frequency range.

## II. GRAPHENE METASURFACES FROM KIRCHHOFF-DIFFRACTION-THEORY VIEWPOINT

We consider a two-dimensional square periodic structure with period $L$ on the dielectric surface coated with a graphene sheet, which is irradiated with a plane electromagnetic wave at normal incidence [see Fig. 1(a) for a sketch and Figs. 1(b)–1(e) for experimental realization of samples].

Kirchhoff's diffraction theory allows us to present the electromagnetic field at arbitrary point $\mathbf{r}$ with the following equation [19]:

$$\begin{aligned}\mathbf{E}(\mathbf{r}) = \int_S \{&[\mathbf{n}' \times \mathbf{E}(\mathbf{r}')] \times \nabla' G(\mathbf{r},\mathbf{r}') \\ &+ [\mathbf{n}' \cdot \mathbf{E}(\mathbf{r}')]\nabla' G(\mathbf{r},\mathbf{r}') \\ &+ i\omega\mu_0[\mathbf{n}' \times \mathbf{H}(\mathbf{r}')]G(\mathbf{r},\mathbf{r}')\}ds', \end{aligned} \tag{1}$$

where $\omega$ is the wave's angular frequency, $\mu_0$ is the vacuum permeability, $\mathbf{n}'$ is the unit vector normal to the surface towards the observation region, and $\nabla' = \partial/\partial\mathbf{r}'$. Vectors $\mathbf{E}(\mathbf{r}')$ and $\mathbf{H}(\mathbf{r}')$ are the electric and magnetic field strengths at the graphene surface, $S$, respectively. The scalar Green function

$$G(\mathbf{r},\mathbf{r}') = \frac{1}{4\pi}\frac{\exp(ik_a|\mathbf{r}-\mathbf{r}'|)}{|\mathbf{r}-\mathbf{r}'|},$$

is determined by the wave number, $k_a = n_a\omega/c$, where subscript $a = 1,2$ labels the refractive index at observation point $\mathbf{r}$.

Equation (1) can be presented in terms of superposition of electromagnetic waves produced by unit cells comprising the surface as

$$\mathbf{E}(\mathbf{r}) = \sum_j \mathbf{E}_j(\mathbf{r}), \tag{2}$$

where

$$\begin{aligned}\mathbf{E}_j(r) = \int_{\rho'\in S_j} \{&[\mathbf{n}' \times \mathbf{E}(\mathbf{r}')] \times \nabla' G(\mathbf{r},\mathbf{r}') \\ &+ [\mathbf{n}' \cdot \mathbf{E}(\mathbf{r}')]\nabla' G(\mathbf{r},\mathbf{r}') \\ &+ i\omega\mu_0[\mathbf{n}' \times \mathbf{H}(\mathbf{r}')]G(\mathbf{r},\mathbf{r}')\}|_{\mathbf{r}'=\boldsymbol{\rho}_j+\boldsymbol{\rho}'}\, d^2\rho'. \end{aligned} \tag{3}$$

Here, integration is taken over area $S_j$ of the $j$th unit cell with the center situated at point $\boldsymbol{\rho}_j$.

In the Fraunhofer approximation, the distance from the center of unit cell $j$ to the observation point, $r_j = |\mathbf{r} - \boldsymbol{\rho}_j|$, is much greater than the size of the unit cell, $L$, and the

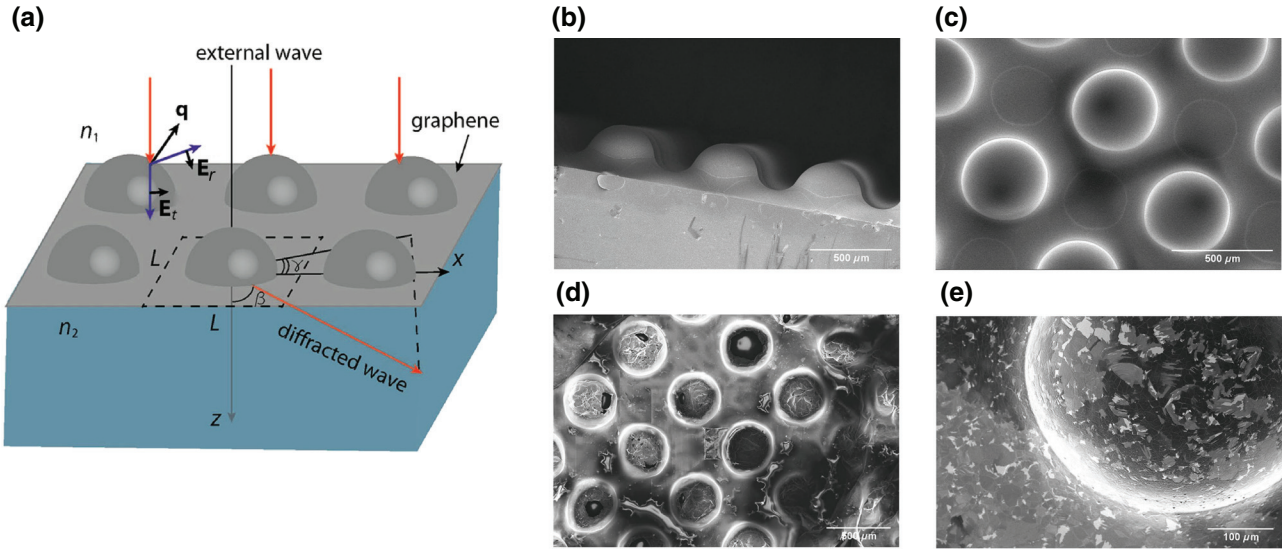


FIG. 1. (a) Sketch of diffraction by a sculptured graphene sheet separating media with refractive indices $n_1$ and $n_2$. (b),(c) SEM images of 3D-printed polymer hemispheres on silica substrate (polymer template). SEM images of the graphene-based metasurface (d) and hemisphere unit cell (e).

Green function and its gradient can be reduced to

$$G(\mathbf{r},\mathbf{r}')|_{\mathbf{r}'=\boldsymbol{\rho}_j+\boldsymbol{\rho}'} = \frac{1}{4\pi}\frac{\exp(ik_a r_j)}{r_j},$$
$$\nabla' G(\mathbf{r},\mathbf{r}')|_{\mathbf{r}'=\boldsymbol{\rho}_j+\boldsymbol{\rho}'} = -\frac{ik_a}{4\pi}\frac{\exp(ik_a r_j)}{r_j}\mathbf{m}_j,$$

where $\mathbf{m}_j = \mathbf{r}_j/r_j$. The electric field emitted by unit cell $j$ equals

$$\mathbf{E}_j(\mathbf{r}) = \frac{ik_a}{4\pi}\frac{\exp(ik_a r_j)}{r_j}\int_{\rho'\in S_j}\{-[\mathbf{n}'\times\mathbf{E}(\mathbf{r}')] \times \mathbf{m}_j - [\mathbf{n}'\cdot\mathbf{E}(\mathbf{r}')]\mathbf{m}_j + Z_a[\mathbf{n}'\times\mathbf{H}(\mathbf{r}')]\}|_{\mathbf{r}'=\boldsymbol{\rho}_j+\boldsymbol{\rho}'}d^2\rho', \quad (4)$$

where $Z_a = Z_0/n_a$ is the wave impedance in ambient medium, $Z_0 = \sqrt{\mu_0/\varepsilon_0}$ is the vacuum impedance, and $\varepsilon_0$ is the vacuum permittivity.

To describe scattering by the metasurface, we will assume the following:

(a) a normal incidence. In such a case, the amplitudes of the electric and magnetic fields at the surface are the same for each unit cell.

(b) (b)that there is no electromagnetic coupling between neighboring cells, i.e., collective excitations (e.g., surface plasmon-polaritons or surface-guided modes) do not occur. In such a case, the light scattered to medium "1" originates from the wave reflected from the metasurface, while the wave scattered into medium "2" originates from the transmitted wave. To find the electric field strength in media 1 (2), we can replace $\mathbf{E}(\mathbf{r}')$ and $\mathbf{H}(\mathbf{r}')$ in Eq. (4) with electric and magnetic fields, respectively, of the wave reflected from (transmitted through) the metasurface at point $\mathbf{r}'$ of the unit cell. Therefore, by taking into account the geometry and material properties of individual cells and summing up contributions of all unit cells, we will obtain the reflectance and transmittance of the metasurface.

Equation (4) is valid for an arbitrary unit-cell geometry; however, it can be considerably simplified for unit cells of high symmetry. In particular, it can be shown that, if the unit cell possesses cylindrical symmetry with respect to the propagation direction of the incident wave, the following relationships hold:

$$\int_{S_c}[\mathbf{n}'\cdot\mathbf{E}(\mathbf{r}')]d^2r' = 0,$$
$$Z_a\int_{S_c}[\mathbf{n}'\times\mathbf{H}(\mathbf{r}')]d^2r' = \mathbf{e}_z\times\int_{S_c}[\mathbf{n}'\times\mathbf{E}(\mathbf{r}')]d^2r', \quad (5)$$

where $S_c$ is the unit-cell area. In the absence of coherency between identical unit cells (no Bragg diffraction), the metasurface spectral properties can be described by the single unit cell with averaged characteristics and the normalized power scattered to the solid angle, $do = \sin\beta d\beta d\gamma$, towards medium 1 ($\pi/2 < \beta < \pi$)

$$\frac{dP^{(1)}}{do}(f,\beta,\gamma) = \frac{|\mathbf{I}^{(1)}(f,\beta,\gamma)|^2\cos\beta}{|\mathbf{E}_i|^2 L^4}, \quad (6)$$

and medium 2 ($0 < \beta < \pi/2$)

$$\frac{dP^{(2)}}{do}(f,\beta,\gamma) = \frac{n_2|\mathbf{I}^{(2)}(f,\beta,\gamma)|^2|\cos\beta|}{n_1|\mathbf{E}_i|^2 L^4}, \quad (7)$$

where $f$ is the wave frequency. Angles $\beta$ and $\gamma$ are introduced in Fig. 1(a). Vectors

$$\mathbf{I}^{(1)} = \int_{S_c}[\mathbf{n}'\times\mathbf{E}_r(\mathbf{r}')]d^2r', \quad \mathbf{I}^{(2)} = \int_{S_c}[\mathbf{n}'\times\mathbf{E}_t(\mathbf{r}')]d^2r', \quad (8)$$

are determined by the distribution of the reflected, $\mathbf{E}_r(\mathbf{r}')$, and transmitted, $\mathbf{E}_t(\mathbf{r}')$, electric field over the unit-cell area.

Reflection and transmission coefficients for the TE and TM (with respect to the element of the unit cell surface) polarized components of the incident wave are equal to

$$r_{\mathrm{TE}}(\alpha_1) = \frac{n_1\cos\alpha_2 - (n_2+\sigma Z_0\cos\alpha_2)\cos\alpha_1}{n_1\cos\alpha_2 + (n_2+\sigma Z_0\cos\alpha_2)\cos\alpha_1},$$
$$r_{\mathrm{TM}}(\alpha_1) = \frac{n_1\cos\alpha_1 - (n_2\cos\alpha_2+\sigma Z_0)}{n_1\cos\alpha_1 + (n_2\cos\alpha_2+\sigma Z_0)},$$
$$t_{\mathrm{TE}}(\alpha_1) = \frac{2n_1\cos\alpha_2}{n_1\cos\alpha_2 + (n_2+\sigma Z_0\cos\alpha_2)\cos\alpha_1},$$
$$t_{\mathrm{TM}}(\alpha_1) = \frac{2n_1\cos\alpha_1}{n_1\cos\alpha_1 + (n_2\cos\alpha_2+\sigma Z_0)}, \quad (9)$$

where $\sigma$ is the graphene surface conductivity, while $\alpha_1$ and $\alpha_2 = \arcsin(n_1\sin\alpha_1/n_2)$ are the local angles of incidence and refraction, respectively. The transmissivity and reflectivity of the metasurface can be obtained by calculating the total energy diffracted into media 1 and 2, respectively, as

$$T(f) = \int_0^{\pi/2}\int_0^{2\pi}\frac{dP^{(2)}}{do}(f,\beta,\gamma)\sin\beta d\beta\, d\gamma,$$
$$R(f) = \int_{\pi/2}^{\pi}\int_0^{2\pi}\frac{dP^{(1)}}{do}(f,\beta,\gamma)\sin\beta d\beta\, d\gamma. \quad (10)$$

## III. UNIT CELLS OF CYLINDRICAL SYMMETRY

We demonstrate [20] that a complex fabrication procedure of a graphene metasurface, involving three-dimensional (3D) printing, electroplating, graphene synthesis, and transfer, allows room for introducing imperfections into the meta-atom structure. In particular, in the fabricated array of graphene hemispheres with characteristic

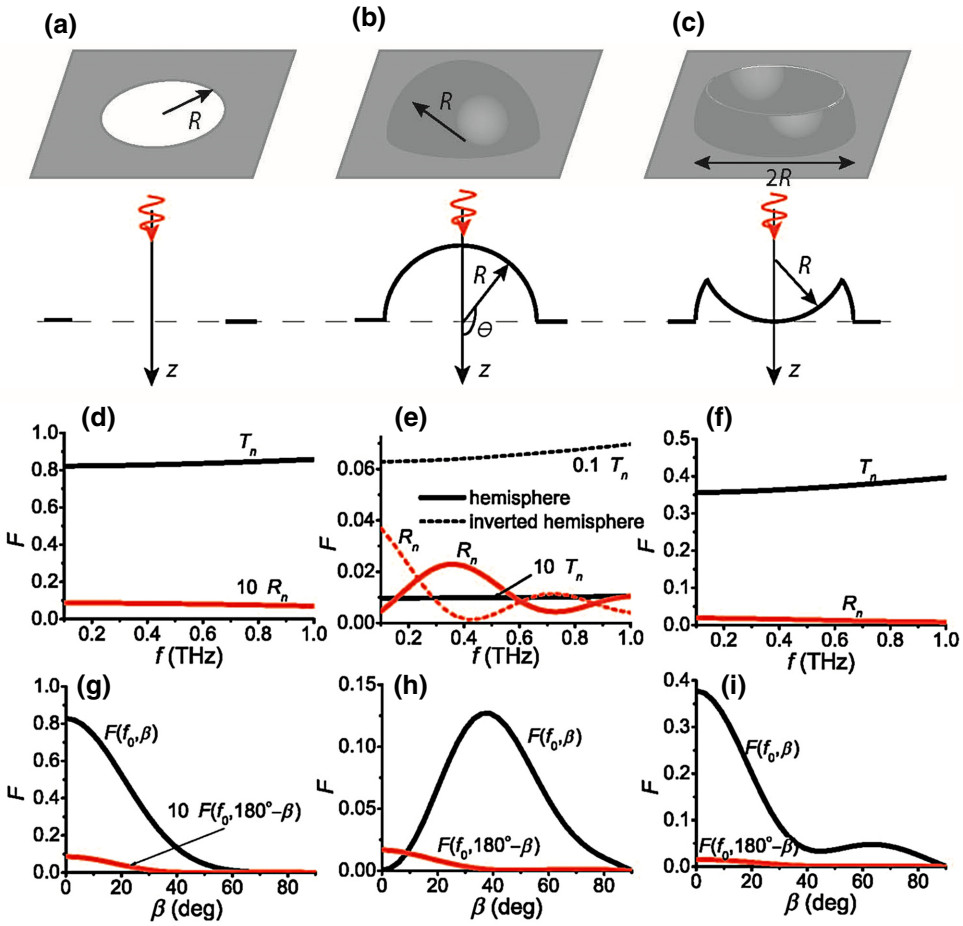


FIG. 2. Normalized power scattered by the metasurface per solid angle, $F(f,\beta) = (dP/do)(f,\beta,0)$, for (a),(d),(g) hole-type, (b),(e),(h) hemisphere-type, and (c),(f),(i) volcanic-type unit cells. Drude-model parameters of graphene are $\mu = 1\ \mathrm{m^2/V}$, $E_F = 0.1$ eV, and $v_F = 10^6$ m/s; geometrical parameters of the metasurface are $L = 611\ \mu$m and $R = 250\ \mu$m; refractive indices of the ambient media are $n_1 = n_2 = 1$; frequency $f_0 = 0.5$ THz. Unit-cell cross sections are shown in the lower parts of (a)–(c).

sizes of 200–600 $\mu$m, a considerable proportion of hemispheres may be completely or partially damaged, being either holes or volcanolike structures, respectively [see Figs. 1(d) and 1(e) for fabricated samples and Fig. 2 for a sketch]. Below, we will calculate the reflectance and transmittance of the metasurface comprising such cylindrically symmetric unit cells, assuming normal incidence.

### A. Hole-type unit cell

The hole-type unit cell, i.e., a hole of radius $R$ in the center of the flat graphene sheet of size $L \times L$, is shown in Fig. 2(a). For the reflected (transmitted) wave, the normal vector of the flat sheet reads $\mathbf{n}' = -\mathbf{e}_z$ ($\mathbf{n}' = \mathbf{e}_z$). To calculate $\boldsymbol{I}^{(1)}$ in Eq. (8), we need to take into account that the graphene-covered and graphene-free areas of the unit cell are $S_{\mathrm{gr}} = L^2 - \pi R^2$ and $S_h = \pi R^2$, respectively, and there is a phase shift owing to the oblique propagation of the diffracted wave propagating in the direction defined by the spherical angles $(\beta, \gamma)$. For the wave diffracted to medium 1, this gives $\mathbf{I}^{(1)}_{\mathrm{hole}} = \mathbf{I}^{(1,hl)} + \mathbf{I}^{(1,fl)}$, where

$$\mathbf{I}^{(1,hl)}(\beta) = -r_0 \frac{2\pi R}{n_1 k_0 \sin\beta} J_1(n_1 k_0 R \sin\beta)[\mathbf{e}_z \times \mathbf{E}_i],$$

$$\mathbf{I}^{(1,fl)}(\beta,\gamma) = -r_g \left\{ \frac{8 \sin[(n_1 k_0 L/2)\cos\gamma \sin\beta]\sin[(n_1 k_0 L/2)\sin\gamma\sin\beta]}{(n_1 k_0 \sin\beta)^2 \sin 2\gamma} - \frac{2\pi R}{n_1 k_0 \sin\beta} J_1(n_1 k_0 R \sin\beta) \right\} [\mathbf{e}_z \times \mathbf{E}_i]. \tag{11}$$

Here, $r_g = [n_1 - (n_2 + \sigma Z_0)]/[n_1 + (n_2 + \sigma Z_0)]$ and $r_0 = (n_1 - n_2)/(n_1 + n_2)$ are reflection coefficients of the graphene-covered and graphene-free areas, respectively, at normal incidence, and $J_1(x)$ is the Bessel function of the first order.

Similarly, for the wave diffracted to medium 2, we arrive at

$$\mathbf{I}^{(2,hl)}(\beta) = t_0 \frac{2\pi R}{n_2 k_0 \ \sin \ \beta} J_1(n_2 k_0 R \ \sin \ \beta)[\mathbf{e}_z \times \mathbf{E}_i]$$
$$\mathbf{I}^{(2,fl)}(\beta,\gamma) = t_g \left\{ \frac{8 \sin[(n_2 k_0 L/2)\cos \ \gamma \ \sin \ \beta] \sin[(n_2 k_0 L/2) \sin \ \gamma \ \sin \ \beta]}{(n_2 k_0 \ \sin \ \beta)^2 \sin \ 2\gamma} - \frac{2\pi R}{n_2 k_0 \ \sin \ \beta} J_1(n_2 k_0 R \ \sin \ \beta) \right\} [\mathbf{e}_z \times \mathbf{E}_i], \tag{12}$$

where $t_g = 2n_1/[n_1 + (n_2 + \sigma Z_0)]$ and $t_0 = 2n_1/(n_1 + n_2)$ are transmission coefficients of the graphene-covered and graphene-free areas, respectively, at normal incidence.

Equations (11) and (12) allow us to obtain the reflectance, $R_n$, and transmittance, $T_n$, in the direction normal to the graphene sheet as

$$R_n(f) = \frac{dP^{(1)}}{do}(f,\pi,0) = \left| r_g + (r_0 - r_g)\frac{\pi R^2}{L^2} \right|^2,$$
$$T_n(f) = \frac{dP^{(2)}}{do}(f,0,0) = \left| t_g + (t_0 - t_g)\frac{\pi R^2}{L^2} \right|^2, \tag{13}$$

when $\sigma Z_0 \ll n_1 = n_2$ and the reflectivity coefficient $r_0 = 0$, while $r_g \approx \sigma Z_0/2n_1$ is low and shows a weak frequency dispersion determined by the Drude-like formula for graphene-surface conductivity [21]:

$$\sigma = \frac{\sigma_0}{1 + i\omega\tau}, \tag{14}$$

where $\sigma_0 = e^2 E_F \tau/\pi\hbar^2$ is the static conductivity, $\tau = \mu\hbar\sqrt{n_s\pi}/ev_F$ is the carrier relaxation time, $n_s = E_F^2/\pi\hbar^2 v_F^2$, $\mu$ is the carrier mobility, $E_F$ is the Fermi energy, and $v_F$ is the Fermi velocity. Figure 2(g) shows that reflected power is small, while the transmitted power maximizes for a normally diffracted wave at $\beta = 0$.

### B. Hemisphere-type unit cell

The hemisphere-type unit cell comprises a graphene hemisphere of radius $R$ in the center of a flat graphene square, $L \times L$ [see Fig. 2(b)]. The wave diffracted into medium 1 is described by $\mathbf{I}^{(1)}_{\text{hemi}} = \mathbf{I}^{(1,fl)} + \mathbf{I}^{(1,hs)}$, where $\mathbf{I}^{(1,fl)}$ was introduced in Eq. (11) and

$$\mathbf{I}^{(1,hs)}(\beta) = -R^2 \int_{\pi/2}^{\pi}\int_0^{2\pi} [\mathbf{e}_r(\theta,\varphi) \times \hat{r}(\pi - \theta)\mathbf{E}_i] e^{i\psi_1(\theta,\beta)} \times \sin \ \theta d\theta d\varphi, \tag{15}$$

Here, $(\pi/2) \le \theta \le \pi$ and $0 \le \varphi < 2\pi$ describe the surface of the hemisphere with radius $R$, as illustrated in Fig. 2(b); $\mathbf{n}' = \mathbf{e}_r(\theta,\varphi)$ is the unit vector of the outward normal of the hemisphere; and $\hat{r}(\theta) = \text{diag}\{r_{\text{TE}}(\theta), r_{\text{TM}}(\theta)\}$ is the reflection coefficient matrix. $\psi_1(\theta,\beta) = n_1 k_0 R[\cos\theta + \cos(\theta - \beta)]$ accounts for a phase of the wave diffracted at the azimuthal angle, $\beta$, with respect to the plane, $z = 0$. Owing to rotational symmetry, the integral $\mathbf{I}^{(1,hs)}$ is $\gamma$ independent.

The electric field of the wave diffracted into medium 2 provides the relationship $\mathbf{I}^{(2)}_{\text{hemi}} = \mathbf{I}^{(2,fl)} + \mathbf{I}^{(2,hs)}$, where $\mathbf{I}^{(2,fl)}$ was introduced in Eq. (12) and

$$\mathbf{I}_1^{(2,hs)}(\beta) = R^2 \int_{\pi/2}^{\pi}\int_0^{2\pi} [\mathbf{e}_r(\theta,\varphi) \times \hat{t}(\pi - \theta)\mathbf{E}_i] e^{i\psi_2(\theta,\beta)} \times \sin\theta d\theta d\varphi. \tag{16}$$

Here, we take into account that, for the transmitted wave, $\mathbf{n}' = -\mathbf{e}_r(\theta,\varphi)$, $\hat{t}(\theta) = \text{diag}\{t_{\text{TE}}(\theta), t_{\text{TM}}(\theta)\}$, and the phase shift $\psi_2(\theta,\beta) = k_0 R[n_2 \cos(\theta - \beta) - n_1 \cos\theta]$.

One can see from Fig. 2(e) that at $\beta = 0$ both normal reflectance, $R_n(f) = (dP^{(1)}/do)(f,0,0)$, and normal transmittance, $T_n(f) = (dP^{(2)}/do)(f,0,0)$, of the hemisphere unit cell are very small. The negligible normal transmissivity can be understood, if one considers that the diffracted field along the $z$ axis originates from projection $\mathbf{p}_\parallel$ on the $X$-$Y$ plane of the net dipole moment induced in graphene by the incident wave. The effective in-plane dipole moment of the unit cell can be presented in the following form:

$$\mathbf{p}_c = \int_{L\times L} \mathbf{p}_\parallel \ e^{i\Delta\psi(x',y')} \frac{dx'dy'}{L^2}, \tag{17}$$

where the phase shift, $\Delta\psi$, takes into account the distance between the hemisphere surface and plane $z = 0$. By introducing the amplitude of the surface current density, $\mathbf{j}_s = -i\omega\mathbf{p}_\parallel$, oscillating at frequency $\omega$ and taking into account that $\mathbf{j}_s = \sigma\mathbf{E}(x',y')$, the dipole moment of the unit cell can be presented in terms of the incident light field as

$$\mathbf{p}_c = \frac{i\sigma_s}{\omega L^2} \int_{L\times L} \hat{t}(x',y')\mathbf{E}_i \ e^{i\Delta\psi(x',y')} \ dx'dy'. \tag{18}$$

Here, $\hat{t}(x',y') = \text{diag}\{t_{\text{TE}}(x',y'), \ t_{\text{TM}}(x',y')\}$ is the transmission coefficient of graphene at point $(x',y')$ of the unit cell.

Figure 3(a) shows the dependence of $|\mathbf{p}_c|$ on the radius, $R$, of holes (black solid line) and hemispheres (red solid

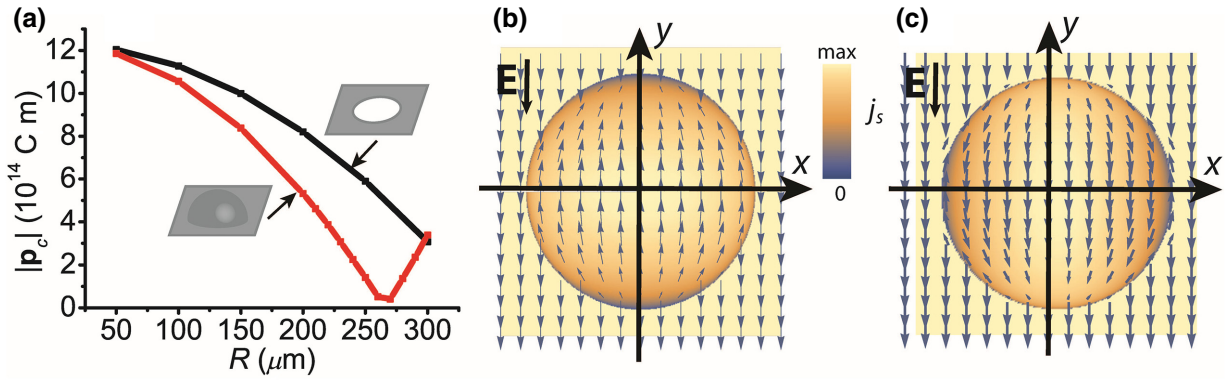


FIG. 3. (a) Absolute value of unit cell's dipole moment $|\mathbf{p}_c|$ as function of radius $R$ of either holes or hemispheres. Distribution of current density $j_s$ projected onto the plane $z=0$ for (b) hemispherical and (c) volcanic unit cells. Parameters are as in Fig. 2.

line). At small $R$, the effective dipole moments of both types of unit cells are approximately equal and close to the dipole moment of flat graphene. Dipole moments decrease with radius; the dependence is not monotonous for hemispheres. Specifically, for the graphene hemisphere, the dipole moment is minimal at $R=265$ $\mu$m. In such a hemisphere, $|\mathbf{p}_c|$ does not exceed 10% of the dipole moment generated in the hole-type unit cells with the same hole radius. This is because the surface current density in the flat graphene area and projection of the current density on the hemisphere surface to the plane, $z=0$, are antiparallel, as demonstrated in Fig. 3(b). If we further increase radius $R$, then the dipole moment of the hemisphere prevails and the absolute value of the net dipole moment increases again, as seen from Fig. 3(a).

The hemisphere inverted with respect to plane $z=0$ exhibits dramatically different properties. In this case, the hemisphere is described by $0 \le \theta \le \pi/2$, while the normal vector, $\mathbf{n}' = -\mathbf{e}_r(\theta,\varphi)$, corresponds to the wave diffracted into medium 1, yielding

$$\mathbf{I}_{\text{inv}}^{(1,hs)}(\beta) = -R^2 \int_0^{\pi/2}\int_0^{2\pi} [\mathbf{e}_r(\theta,\varphi)\times\hat{r}(\theta)\mathbf{E}_i] e^{i\psi_1(\theta,\beta)} \times \sin\theta d\theta d\varphi. \tag{19}$$

It worth mentioning that the phase function, $\psi_1(\theta,\beta)$, does not change.

Normal transmittance, $T_n$, and reflectance, $R_n$, of the metasurface with inverted hemispheres are demonstrated in Fig. 2(e) with dashed lines. The magnitudes of $R_n$ are comparable for hemispheres and their inverted counterparts, but the maxima and minima change over. At the same time, the value of $T_n$ significantly increases, more than 100 times compared to the case of normal hemispheres.

Although normal transmittance, $T_n$, is very low for hemispheres, the scattered power to medium 2 can be quite large. From Fig. 2(h), one can observe that the scattered power is maximal near $\beta = 40^\circ$, indicating that considerable light energy can be diffracted at nonzero angles, while the reflected power, which is determined by the graphene-surface conductivity, remains small for all diffraction angles.

### C. Volcanic type unit cell

The third type of unit cell we consider is a broken hemisphere, in which the upper segment falls down, forming a sort of volcano crater, as shown in Fig. 2(c). The volcanolike shape is composed of two segments. The first one, $\pi/2 \le \theta \le 2\pi/3$, is the remainder of the initial hemisphere characterized by the normal vector, $\mathbf{n}' = \mathbf{e}_r$, for the waves diffracted to medium 1. The second segment, $0 \le \theta \le \pi/3$, is part of the sphere centered at $z=-R$; its normal vector is $\mathbf{n}' = -\mathbf{e}_r$. Thus, the integral describing diffraction to medium 1 is $\mathbf{I}_{\text{volcano}}^{(1)} = \mathbf{I}^{(1,fl)} + \mathbf{I}^{(1,\text{vol})}$, where

$$\begin{aligned}\mathbf{I}^{(1,\text{vol})}(\beta) = {} & R^2 \int_{\pi/2}^{2\pi/3}\int_0^{2\pi} [\mathbf{e}_r(\theta,\varphi)\times\hat{r}(\pi-\theta)\mathbf{E}_i] \\ & \times e^{i\psi_1(\theta,\beta)}\sin\theta d\theta d\varphi \\ & - R^2 \int_0^{\pi/3}\int_0^{2\pi} [\mathbf{e}_r(\theta,\varphi)\times\hat{r}(\theta)\mathbf{E}_i] \\ & \times e^{i\psi_1(\theta,\beta)-2ikR}\sin\theta d\theta d\varphi.\end{aligned} \tag{20}$$

For calculation of the transmittance, we need to reverse the normal vector, $\mathbf{e}_r(\theta,\varphi) \to -\mathbf{e}_r(\theta,\varphi)$, and replace $\psi_1(\theta,\beta)$ and $\psi_1(\theta,\beta) - 2kR$ with $\psi_2(\theta,\beta)$.

Dependences of the scattered power on the frequency and diffraction angle are quite similar to those for the hole-type metasurface, compare Figs. 2(d) and 2(f), and 2(g) and 2(i). However, the magnitudes of the scattered power are lower for volcano craters. The distribution of the forward-scattered power in Fig. 2(i) has an intensive tail for $\beta > 40^\circ$. The enhanced scattering of volcanic-type metasurfaces is supported by the distribution of the current density in Fig. 3(c) showing that, in this case, the

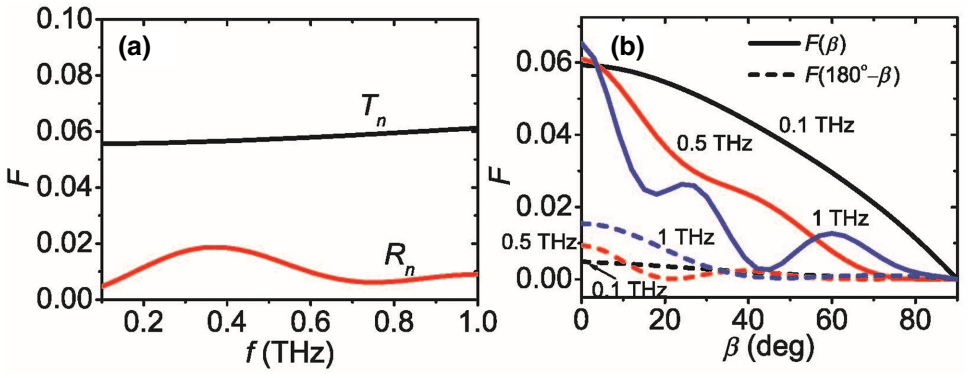


FIG. 4. (a) Power $F = dP/do$ scattered normally to the metasurface in the forward $T_n$ and backward $R_n$ directions. (b) Power $F(\beta)$ scattered by the metasurface over the whole range of diffraction angles for 3 frequencies, $f_0 = 0.1$, 0.5, and 1 THz. Parameters of the unit cells are given in Fig. 2, while the weight factors are $w_1 = 0.6$, $w_2 = 0.35$, and $w_3 = 0.05$.

dipole moment of the unit cell gives rise to the high transmissivity.

## IV. RANDOM METASURFACES

Inevitable fabrication defects break long-range order in the two-dimensional array of meta-atoms and may essentially affect the performance of the metasurface. In this section, we will estimate to what extent the hole- and volcano-type defects are capable of affecting the diffracted field. Specifically, we assume that the probabilities of finding an undamaged hemisphere, hole-type defect, and volcano-type defect in particular position of the meta-atom array are $w_1$, $w_2$, and $w_3$, respectively, where $w_1 + w_2 + w_3 = 1$. In such a case, the reflectivity can be found by averaging the electric field scattered by the meta-atoms into medium 1, i.e., by replacing $\mathbf{I}^{(1)}(f, \beta, \gamma)$ in Eq. (6) with

$$\mathbf{I}^{(1)} = w_1 \mathbf{I}^{(1)}_{\text{hemi}} + w_2 \mathbf{I}^{(1)}_{\text{hole}} + w_3 \mathbf{I}^{(1)}_{\text{volcano}}. \tag{21}$$

Since each unit cell also includes a flat graphene-covered substrate, we can present the energy diffracted into medium 1 in terms of the integrals introduced in the previous section as

$$\begin{aligned}\mathbf{I}^{(1)} &= w_1[\mathbf{I}^{(1,fl)} + \mathbf{I}^{(1,hs)}] + w_2[\mathbf{I}^{(1,fl)} + \mathbf{I}^{(1,hl)}] \\ &\quad + w_3[\mathbf{I}^{(1,fl)} + \mathbf{I}^{(1,\text{vol})}] \\ &= w_1\mathbf{I}^{(1,hs)} + w_2\mathbf{I}^{(1,hl)} + w_3\mathbf{I}^{(1,\text{vol})} + \mathbf{I}^{(1,fl)}.\end{aligned} \tag{22}$$

To find the power diffracted into medium 2, we should change superscript 1 to 2, i.e., $\mathbf{I}^{(1,hs)} \to \mathbf{I}^{(2,hs)}$, and so on.

In the following analysis, we assume $w_1 = 0.6$, $w_2 = 0.35$, and $w_3 = 0.05$, which correspond to the metasurface studied in Ref. [20]. Comparing the results of modeling presented in Fig. 4(a) with those in Figs. 2(d)–2(f), one may conclude that, at $\beta = 0°$, the hemisphere-type unit cells dominate the transmittance and reflectance of the random metasurface. Our analysis shows that relative contribution of volcano- and hole-type unit cells essentially depends on frequency. The angular dependences in Fig. 4(b) allow one to observe characteristic peaks featuring contributions of a particular type of unit cell, the responses of which are given in Figs. 2(g)–2(i). At $f_0 = 0.5$ THz, we see the contribution of the volcano-type unit cell as a maximum at $\beta = 0°$ and the contribution of the hemisphere-type unit cell as a weak peak near $\beta = 40°$.

Spectra of the reflectivity and transmissivity calculated using Eq. (10), i.e., the total relative power scattered to media 1 and 2, are illustrated in Fig. 5. While the reflectivity is low over the whole frequency range, the transmissivity increases up to 18% at 0.1 THz because $(dP^{(2)}/do)(f, \beta, \gamma)$ increases when the frequency decreases [see Fig. 4(b)]. The absorptivity, $A = 1 - R - T$, of the graphene metasurface exceeds 80% in the spectral range from 0.1 to 1 THz and 90% from 0.5 to 1 THz and is as high as 94% at 1 THz. Such a strong absorption performance is surprising when considering that a noticeable proportion of the damaged meta-atoms destroys the low-range order in the array. It is important that the considered random metasurface is a broadband absorber due to the suppressed dipole moment and, therefore, transmissivity.

It is worth noting that transmittance and reflectance for the wave diffracted normally to the metasurface, $T_n(f) = (dP^{(2)}/do)(f, 0, 0)$ and $R_n(f) = (dP^{(1)}/do)(f, 0, 0)$, resp-

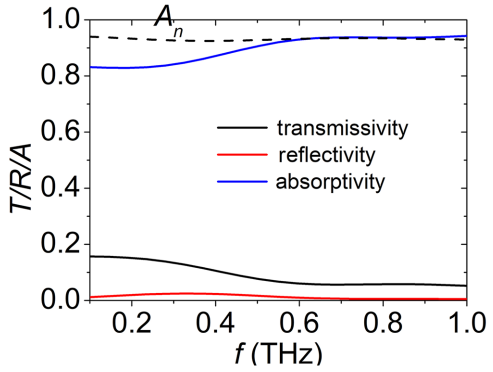


FIG. 5. Reflectivity, transmissivity, and absorptivity of the random metasurface in Fig. 4. Dashed line demonstrates the absorptivity, which is calculated as $A_n = 1 - T_n - R_n$.

ectively, can be used for a reasonable estimation of the absorptivity, according to $A \approx 1 - T_n - R_n$ (see Fig. 5). In the case of oblique incidence, the reflectivity stays small due to the low graphene conductivity, while the transmissivity may significantly increase owing to the non-negligible dipole moment of the unit cell. In such a case, the absorptivity of the random graphene metasurface will be suppressed.

## V. RESULTS AND DISCUSSION

### A. Comparison to experiment

Samples of a free-standing metasurface composed of graphene hemispheres are fabricated as described in Ref. [20], see Figs. 1(b)–1(e). Briefly, a 3D-printed array of polymer hemispheres is sputtered on a nanometer-thick Ni layer for further electroplating to fabricate the nickel pattern used for CVD synthesis of multilayered graphene. The graphene metasurface is then coated with 200 nm of polymethylmethacrylate (PMMA) for safe transfer to the membrane holder.

The metasurface is typically composed of 55%–60% of ideal hemispheres ($w_1 = 0.6$), 30%–40% of volcano meta-atoms ($w_2 = 0.35$), and 5%–10% of hole meta-atoms ($w_3 = 0.05$).

Details of the THz time-domain setup and THz measurements can be found in Ref. [22,23].

To compare results of the experiment with predictions of the developed model, we take into account that the PMMA film thickness is much smaller than the wavelength, i.e., we may consider the graphene metasurface in free space ($n_1 = n_2 = 1$). To account for the piecewise nature of multilayered graphene made on the electroplated Ni template [20], comprising single- and two-layer graphene domains, we modify Eq. (14) for the surface conductivity as follows:

$$\sigma_s^{\text{eff}} = Y\frac{\sigma_0}{1 + i\omega\tau} \tag{23}$$

where $Y = \alpha_1 + 2\alpha_2$; $\alpha_1$ and $\alpha_2$ are the weight factors of the single-layer and two-layer graphene areas ($\alpha_1 + \alpha_2 = 1$).

Figure 6 shows measured and calculated dependences of the diffracted power on the frequency and diffraction angle. One can observe from Fig. 6(a) that theory reproduces the measured transmittivity with about 20% accuracy over the whole spectrum range. Figures 6(b)–6(d) demonstrate that the modeling predict a general trend in the dependence of $(dP^{(2)}/do)(\beta)$ on diffraction angle $\beta$, which can serve as a validation of the applied averaging procedure on the geometry of unit cells.

### B. Absorptivity optimization

In this subsection, we will investigate the influence of all parameters (graphene conductivity, metasurface geometry, and perfectness) on the metasurface absorptivity, $A$, which is of paramount practical importance. One can see from Fig. 7(a) that, to increase absorptivity, one needs to reduce the Fermi energy, i.e., the doping level of graphene should be moderate. In such a case, the surface conductivity and reflectivity will be low, whereas the transmissivity can

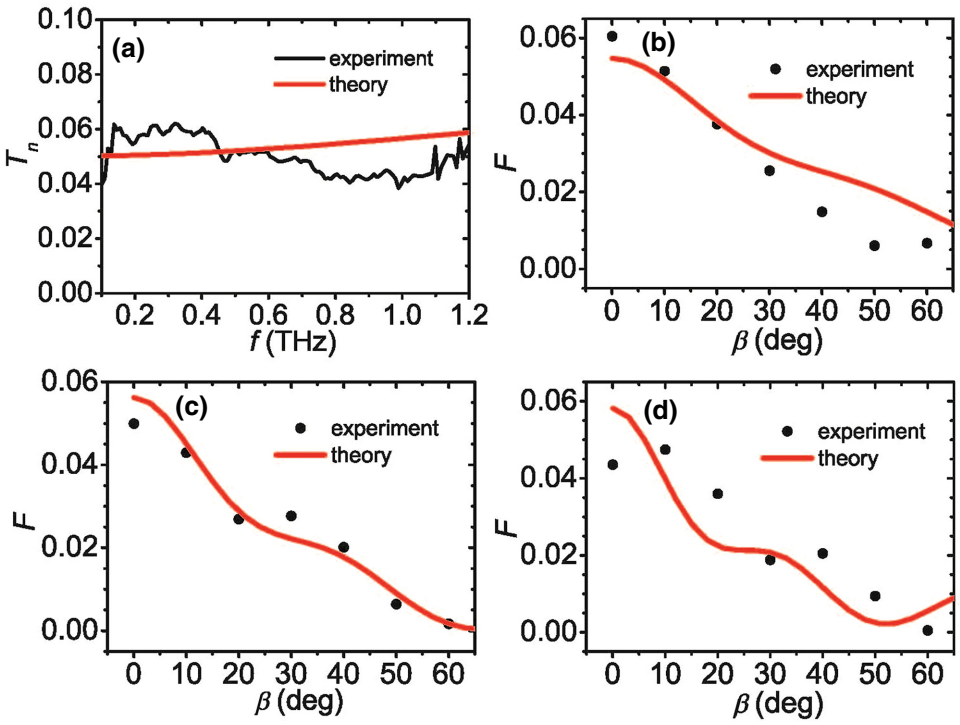


FIG. 6. Frequency dependence of the metasurface normal transmittance, $T_n$ (a), and scattered normalized power, $F = dP^{(2)}/do$, vs diffraction angle, $\beta$, at (b) 0.4 THz, (c) 0.6 THz, and (d) 0.8 THz. Solid red lines represent predictions of the developed theory, while black solid line and black dots show experimental data. Metasurface parameters are shown in the caption of Fig. 4. Graphene-surface conductivity is calculated from Eq. (23), assuming layering weight factors $\alpha_1 = 0.7$ and $\alpha_2 = 0.3$.

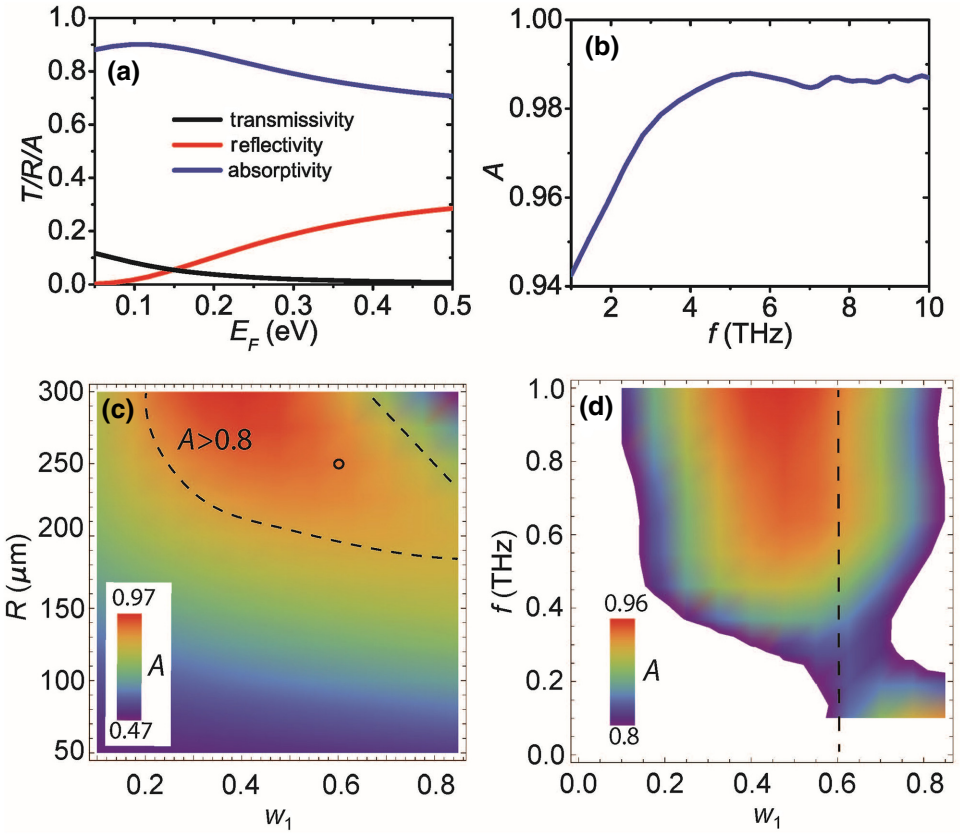


FIG. 7. (a) Transmissivity, reflectivity, and absorptivity as functions of the Fermi energy at $f_0 = 0.5$ THz. (b) Absorptivity $A$ vs frequency at $E_F = 0.1$ eV. Absorptivity as a function of a couple of parameters: (c) $A(w_1, R)$ and (d) $A(w_1, f)$. We adopt parameters as in Fig. 4. In (c), dashed lines distinguish the area of high absorptivity ($A > 0.8$). Circle in (c) and vertical dashed line in (d) mark the experimental parameters.

be suppressed due to tailoring of the unit-cell geometry. For higher Fermi energies, the conductivity and reflectivity increase, while the transmissivity decreases, leading to suppression of the absorptivity. Therefore, typical for the CVD graphene/PMMA sandwich [23], a Fermi energy of $E_F = 0.1$ eV is appropriate to achieve a high absorptivity.

The absorptivity as a function of frequency, as demonstrated in Fig. 5, indicates that, the higher the frequency, the higher the absorptivity. Figure 7(b) shows that the absorptivity is very close to the perfect one at $f > 5$ THz. At high frequencies, the transmissivity peaks in the vicinity of $\beta = 0$ (geometrical optics limit), i.e., the transmittivity coincides with the transmittance at normal incidence, $T \approx T_n$, and, therefore, the absorptivity is well estimated by $A \approx A_n$. Furthermore, we fix the value of the frequency, $f_0 = 0.5$ THz, and determine the maximal value of the absorptivity, $A(R, w_1)$, as a function of these two parameters.

Figure 7(c) presents a map of the absorptivity as a function of hemisphere radius $R$ and proportion of perfect hemispheres in the array, $w_1$. At small radii $R$, the dipole moment of the meta-atom does not vanish and, therefore, the transmissivity is noticeable. At bigger radii, the dipole moment and transmissivity can be minimized at some value of $w_1$, thus maximizing the absorptivity. The default parameters ($w_1 = 0.6$ and $R = 250$ $\mu$m) marked with a circle in the figure are within the region of high absorptivity, $A > 0.8$, highlighted by the dashed line in Fig. 7(c). Figure 7(d) shows the density plot of absorptivity as a function of $f$ and $w_1$ at a hemisphere radius of $R = 250$ $\mu$m. One can see that the absorptivity is high over a wide range of $w_1$ and $f$ and rapidly decreases at lower frequencies.

There are no strict limitations on the spacing between unit cells $L$, because the effect of near-perfect absorptivity we discuss is not related to excitation of the resonance modes. The frequency window, in which the metasurface absorber works, is restricted by the increase of graphene's conductivity and, therefore, reflectivity at lower frequencies and the influence of interband transitions at higher frequencies. According to Ref. [24], the intraband contribution dominates over the interband one for wavelengths greater than approximately 30 $\mu$m (at frequencies $f < 10$ THz). The Drude model for graphene can be applied only up to this frequency, showing a high absorptivity in Fig. 7(b).

## VI. CONCLUSION

We present an approach to describe random metasurfaces. The broken periodicity of the meta-atom array allows us to describe the diffraction problem in terms of the scattering of individual meta-atoms. The developed

theory can be applied to any random or nonperfect electromagnetic metasurfaces composed of isotropic, anisotropic, chiral, and bianisotropic unit cells, acting at wavelengths where the Bragg resonances are suppressed.

We apply this strategy to a random graphene metasurface containing three types of meta-atoms originating from the imperfection of the fabrication process (perfect hemispheres and hole- and volcano-type defects). A broadband-absorbing random graphene metasurface is chosen as a good experimentally realized example to show the applicability of the developed diffraction theory and how efficient it might be for optimizing the fabrication or synthesis parameters.

The theory is well suited to experimental measurements, as demonstrated in Fig. 6, provided that (i) there is no electromagnetic coupling between the meta-atoms, and (ii) the number of meta-atoms of each type is large enough to break the periodicity. The developed theory and experimental results show that the free-standing random graphene metasurface exhibits an outstanding absorption ability.

The close-to-perfect absorptivity is broadband and highly tolerant to variation of the geometric and material parameters. Thus, defective fabrication may enhance the absorption performance of the metasurface, providing researchers with a broadband absorber in the THz range.

## ACKNOWLEDGMENT

This work is supported by the Academy of Finland via Flagship Programme Photonics Research and Innovation (PREIN), Decision No. 320166 and Grant No. 343393, and the Horizon 2020 RISE DiSeTCom Project No. 823728.

[1] H.-T. Chen, A. J. Taylor, and N. A. Yu, Review of metasurfaces: Physics and applications, Rep. Prog. Phys. **79**, 076401 (2016).

[2] S. B. Glybovski, S. A. Tretyakov, P. A. Belov, Y. S. Kivshar, and C. R. Simovski, Metasurfaces: From microwaves to visible, Phys. Rep. **634**, 1 (2016).

[3] F. Ding, A. Pors, and S. I. Bozhevolnyi, Gradient metasurfaces: A review of fundamentals and applications, Rep. Prog. Phys. **81**, 026401 (2018).

[4] O. Quevedo-Teruel, *et al.*, Roadmap on metasurfaces, J. Opt. **21**, 073002 (2019).

[5] W. T. Chen, A. Y. Zhu, and F. Capasso, Flat optics with dispersion-engineered metasurfaces, Nat. Rev. Mater. **5**, 604 (2020).

[6] N. Yu, P. Genevet, M. A. Kats, F. Aieta, J.-P. Tetienne, F. Capasso, and Z. Gaburro, Light propagation with phase discontinuities: Generalized laws of reflection and refraction, Science **334**, 333 (2011).

[7] E. Hasman, G. Biener, A. Niv, and V. Kleiner, Space-variant polarization manipulation, Prog. Opt. **47**, 215 (2005).

[8] C. Pfeiffer and A. Grbic, Metamaterial huygens' surfaces: tailoring wave fronts with reflectionless sheets, Phys. Rev. Lett. **110**, 197401 (2013).

[9] B. Sensale-Rodriguez, R. Yan, M. M. Kelly, T. Fang, K. Tahy, W. S. Hwang, D. Jena, L. Liu, and H. G. Xing, Broadband graphene terahertz modulators enabled by intraband transitions, Nat. Commun. **3**, 780 (2012).

[10] H. Chen, W.-B. Lu, Z.-G. Liu, and M.-Y. Geng, Microwave programmable graphene metasurface, ACS Photonics **7**, 1425 (2020).

[11] S. R. Biswas, C. E. Gutiérrez, A. I.-H. Nemilentsau, I.-H. Lee, S.-H. Oh, P. Avouris, and T. Low, Tunable graphene metasurface reflectarray for cloaking, illusion, and focusing, Phys. Rev. Appl. **9**, 034021 (2018).

[12] G. Hu, A. Krasnok, Y. Mazor, C.-W. Qiu, and A. Alù, Moiré hyperbolic metasurfaces, Nano Lett. **20**, 3217 (2020).

[13] R.-H. Xiong, X. Q. Peng, and J.-S. Li, Graphene-metasurface for wide-incident-angle terahertz absorption, Front. Inf. Technol. Electron. Eng. **22**, 334 (2021).

[14] S. Lee, H. Heo, and S. Kim, Graphene perfect absorber of ultra-wide bandwidth based on wavelength-insensitive phase matching in prism coupling, Sci. Rep. **9**, 11967 (2019).

[15] X. Cheng, R. Huang, J. Xu, and X. Xu, Broadband terahertz near-perfect absorbers, ACS Appl. Mater. Interfaces **12**, 33352 (2020).

[16] X. Li, G. Feng, and S. Lin, Ultra-wideband terahertz absorber based on graphene modulation, Appl. Opt. **60**, 3170 (2021).

[17] E. Galiffi, J. B. Pendry, and P. A. Huidobro, Broadband tunable THz absorption with singular graphene metasurfaces, ACS Nano **12**, 1006 (2018).

[18] M. Dupré, L. Hsu, and B. Kanté, On the design of random metasurface based devices, Sci. Rep. **8**, 7162 (2018).

[19] J. D. Jackson, *Classical Electrodynamics* (John Wiley & Sons, New York, 1999).

[20] M. Baah, A. Paddubskaya, A. Novitsky, N. Valynets, M. Kumar, T. Itkonen, M. Pekkarinen, E. Soboleva, E. Lahderanta, M. Kafesaki, Y. Svirko, and P. Kuzhir, All-graphene perfect broadband THz absorber, Carbon **185**, 709 (2021).

[21] A. Ferreira, J. Viana-Gomes, Y. V. Bludov, V. Pereira, N. M. R. Peres, and A. H. Castro Nero, Faraday effect in graphene enclosed in an optical cavity and the equation of motion method for the study of magneto-optical transport in solids, Phys. Rev. B **84**, 235410 (2011).

[22] A. Paddubskaya, N. Valynets, S. Maksimenko, M. Kumar, M. Baah, M. Pekkarinen, Y. Svirko, G. Valusis, and P. Kuzhir, THz photonics with graphene enhanced polymer hemispheres array, Nanomaterials **11**, 2494 (2021).

[23] K. Batrakov, P. Kuzhir, S. Maksimenko, N. Volynets, S. Voronovich, A. Paddubskaya, G. Valusis, T. Kaplas, Y. Svirko, and Ph. Lambin, Enhanced microwave-to-terahertz absorption in graphene, Appl. Phys. Lett. **108**, 123101 (2016).

[24] N. K. Emani, A. V. Kildishev, V. M. Shalaev, and A. Boltasseva, Graphene: A dynamic platform for electrical control of plasmonic resonance, Nanophotonics **4**, 214 (2015).